Journal of Hazardous Materials Advances 8 (2022) 100163

Contents lists available at ScienceDirect

Journal of Hazardous Materials Advances

journal homepage: www.elsevier.com/locate/hazadv

Weed to nano seeds: Ultrasonic assisted one-pot fabrication of superparamagnetic magnetite nano adsorbents from Siam weed flower extract for the removal of lead from water.

Julia Garvasis [a], Anupama R. Prasad [a], K.O. Shamsheera [a], T.A. Nidheesh Roy [b], Abraham Joseph [a,*]

[a] Department of Chemistry, University of Calicut, Calicut University, P O-673 635, India
[b] Department of Biotechnology, University of Calicut, Calicut University, P O, 673 635, India

ARTICLE INFO

Keywords:
Ultra-small
Superparamagnetic magnetite NPs
Weed to seed
Langmuir adsorption isotherm

ABSTRACT

A novel phyto-conjugated magnetite nanoadsorbent with appreciable adsorption capacity, minimal ionic interference, and economic reusability for the selective removal of Pb(II) in aqueous solutions have been proposed in this study. PXRD, SEM, surface charge analysis, XPS, TEM and vibrating sample magnetometry were used for the characterization of ultrasmall superparamagnetic magnetite nanoparticles (USMNs). The effect of contact time, adsorbent dosage, initial concentration of the pollutants, temperature, and pH on adsorption efficiency was investigated via adsorption batch experiments. It was observed that the pH of the medium controlled the adsorption process. The equilibrium for the adsorption of Pb(II) ions followed the Langmuir isotherm model. The maximum adsorption capacity recorded was **315.43 mg g^{-1}** for Pb(II) ions. The adsorption process conformed well to pseudo first order kinetics as revealed by the high R^2 value. The thermodynamic parameters revealed that the adsorption of Pb(II) ions onto the nanoadsorbents was spontaneous, feasible, and endothermic under the applied conditions. Exhausted USMNs were recovered by pH management and 92% efficiency was retained after 5 consecutive cycles.

1. Introduction

The boom in anthropogenic activities and improper handling of resources have caused an alarming hike of heavy metal ions in the ecosystem. The hazards caused by lead are more extensive than any other pollutant out there. Though the use of leaded petrol has been restricted in many countries, the metal is still found in several other products including paint, plumbing pipes, ceramics, pottery glaze, cosmetics, and batteries. Reports have revealed the use of lead in food adulteration and traditional medicines (Kapoor and Singh, 2021; Obeng-Gyasi, 2019). Lead is a highly poisonous, cumulative contaminant that persists at the disposal site as a source of exposure for long periods. Even the lowest measurable blood lead levels can compromise the reproductive, neurological, and cardiovascular systems of an adult. Chronic and high lead exposure can cause hematological effects and neurological disturbances, lethargy, muscle weakness, ataxia, tremors and paralysis, and even death (Wani et al., 2015). Compared to adults, children are more vulnerable to the irreversible adversities of lead exposure. Neurological disorders, retarded growth, and juvenile delinquency are closely associated with infantile lead exposure (Naranjo et al., 2020). Lead is a recyclable metal therefore the establishment of safe and efficient recycling infrastructures can help in regulating the lead levels in water and soil (Reck and Graedel, 2012; Zhang et al., 2016).

Recently, several physicochemical methods have been used for the removal of lead and other heavy metal ions from polluted water, such as chemical precipitation (Xu et al., 2021), ion exchange (Murray and Örmeci, 2019), membrane filtration, reverse osmosis, coagulation, and adsorption (Khulbe and Matsuura, 2018; Fu and Wang, 2011). Among these techniques, the adsorption method is highly preferred due to its cost-effectiveness, flexibility of materials, and easy execution. An efficient adsorbent should possess appreciable selectivity, high adsorption capacity, and be recyclable (Bolisetty et al., 2019). Although adsorption is widely used to remove lead ions from water, fabrication of promising adsorbent systems is very challenging due to multiphase synthesis routes and the expensive chemicals involved. Another demerit of the adsorption process is the laborious separation of the exhausted adsorbent at the end of the process. Usually, multiple centrifugations or filtration steps are performed to separate the analyte free of the loaded adsorbent. In this regard, iron oxide nanoparticles are highly exploited for their magnetic properties which provide fast separation and easy re-

* Corresponding author.
E-mail address: abrahamjoseph@uoc.ac.in (A. Joseph).

https://doi.org/10.1016/j.hazadv.2022.100163
Received 29 July 2022; Received in revised form 4 September 2022; Accepted 6 September 2022

generation under an external magnetic field (Mehta et al., 2015). However pure iron oxide NPs are prone to agglomeration which decelerates their absorption capacity (Muthukumaran and Philip, 2016). Surface reformations using suitable surfactants, biomolecules, and polymers are a viable approach to enhance the adsorption efficiency (Ali et al., 2016). There are substantial reports on the use of crude phytoextracts for the synthesis of iron oxide nanoparticles. The plant metabolites (polyphenols, amino acids, polysaccharides, alkaloids) present in these phytoextracts act as effective reducing and capping agents. The incorporation of organic functional groups onto the phytogenic nanoparticle surface makes it a potential candidate for the recovery of aqueous heavy metal ions (Ali et al., 2017). Recently many researchers have reported phytogenic synthesis of iron oxide nanoparticles using leaf extracts (Groiss et al., 2017), fruit peel extracts (Yusefi et al., 2020), and seed extracts (Bibi et al., 2019). However, attaining desired particle size and monodispersed morphology remains the most challenging part of phytogenic synthesis (Roy et al., 2022).

Herein we report a facile green synthesis strategy for monodispersed magnetite nanoparticles employing *Chromolaena odorata (L) King & Robins,* commonly known as siam weed for the removal of Pb(II) from contaminated water. Siam weed is an invasive, allelopathic tropical species that cause severe impacts on the eco-diversity during its propagation (Aigbedion-Atalor et al., 2019). The plant was introduced to tropical Asia, West Africa, and parts of Australia where it is considered as a noxious weed and is listed in the 100 of the world's worst invasive alien species by the Global Invasive Species Database (IUCN, GISD) (Lowe et al., 2000). The ability of the plant to thrive in a wide range of soils and habitats makes it a nuisance weed in agricultural and commercial plantations. Clearing out large bushes of siam weed has become an expensive annual ritual for land owners (Cuthbert et al., 2022). However, most of the control methods are ineffective due to the high germination potential of the seeds. Therefore, a sustainable alternative would be exploring the plausible uses of the plant in different fields (Sajeev et al., 2012). Siam weed extracts are reported to possess appreciable antioxidant properties, iron chelation ability, antimicrobial properties, and minimal cytotoxic effects. The plant is widely used in traditional medicine against several ailments and wound healing (Eze and Jayeoye, 2021; Vijayaraghavan et al., 2017). However, there are no reports on the reductive and capping abilities of the siam weed flower extracts. Our work studies the simultaneous use of the siam weed flower extract (SWE) as a reductant and a capping agent in the synthesis of magnetite nanoparticles. Adsorptive properties of the obtained siam weed-derived superparamagnetic magnetite nanoparticles towards Pb(II) contaminated water was extensively studied. Moreover, the foraging of the flowers can help in controlling the invasion of Siam weed to more areas.

2. Materials and methods

2.1. Materials

Analytical grade $FeCl_3.6H_2O$, (99.8% purity), $NaHCO_3$ (98% purity), and $Pb(NO_3)_2$ (98% purity) were purchased from Merck and used as obtained. Siam weed flowers were foraged locally from in and around the University of Calicut, Kerala. For future reference, a voucher specimen was deposited in Calicut University Herbarium (CALI) (voucher ID 7086). Fresh, healthy flowers were cleansed thoroughly under tap water and air-dried naturally, before extraction of the plant metabolites.

2.2. Synthesis of iron oxide nanoparticles

To 350 ml of deionized water kept at 80 °C, 20 g of dried flowers were added and vigorously mixed using a magnetic stirrer. The temperature of the system was maintained at 40 °C overnight for effective extraction of phytochemicals. The cooled mixture was then strained through a two-fold muslin cloth to obtain the siam weed extract (SWE). Qualitative phytoscreening of SWE was conducted and total phenolic content and flavonoid content were estimated using standard analytical techniques (Ainsworth and Gillespie, 2007; Usman et al., 2009). To 50 ml of the SWE, 30 ml of 0.032 M $FeCl_3$ solution was added under vigorous magnetic stirring. The decline in the pH of the medium was adjusted by the gradual addition of 0.52 g of $NaHCO_3$. The resultant black solution was homogenized using Branson 150 D Sonifier with an immersed ultrasonic probe (2.38 mm, 25 kHz) for 15 min and was then magnetically stirred for 1 h at room temperature. The mixture was then exposed to hydrothermal treatment at 180 °C for 8 h in a teflon-lined autoclave. The black, solid product formed was magnetically separated, and sequentially washed with ethanol and water to remove any adhered reactant residues. The slurry was then dried at 70 °C in an air oven to obtain USMNs. The procedure excluding the ultrasonication step was repeated on another set of reactants to study the effect of ultrasonic homogenization on the formed superparamagnetic magnetite nanoparticles (SMNs).

2.3. Characterization of USMNs and SMNs

The powder X-ray diffraction patterns of USMNs and SMNs were measured (PXRD) on a Malvern-PanAnalytical X-ray diffractometer. The Scherrer equation was used to compute the crystallite size of the particles from the PXRD profile. Fourier transform infrared spectroscopy measurements were performed (JASCO FTIR- 4600 spectrophotometer) for primary assessment of functional groups in SWE and obtained products. The morphology of both USMNs and SMNs was inspected under **a Carl-Zeiss (Sigma) field emission scanning electron microscope** and high-resolution transmission electron microscope (Jeol/JEM 2100). The magnetic properties were examined using Lakeshore VSM 7410 vibrating sample magnetometer at 298 K. Zeta potential measurements (Brookhaven PALS zeta potential analyzer Ver.5.60) were conducted to estimate the surface charges on formed nanoparticles. X-ray photoelectron spectroscopy (Omicron Nanotechnology) and EDX analysis (Bruker, Nano XFlash Detector) were used for an in-depth investigation of surface elemental composition, valence state, and mechanism of lead removal by USMNs.

2.4. Adsorption batch experiments

A stock solution of $Pb(NO_3)_2$ (500 mg L^{-1}) was prepared. Effluents for the study were simulated by diluting the stock solution with known volumes of deionized water. Adsorption batch studies were conducted in glass vessels kept on a platform shaker. The adsorption experiments were performed by dispersing USMNs/SMNs (1.5 g L^{-1}) into 20 ml of Pb(II) solution (100 mg L^{-1}). The adsorbents were separated using an external magnet and supernatant solution was retrieved at regular contact intervals. The procured sample was analysed using atomic absorption spectroscopy (Shimadzu AA 7000) for residual Pb(II) concentration **and for iron leaching**. The contact time for USMNs and SMNs was optimized to identify the most suitable adsorbent for aqueous Pb(II) removal. The effect constraints including pH, temperature and initial concentration of Pb(II) on the adsorption capacity of both adsorbents were also investigated. The effect of pH was studied in the range of pH 2-7. A Mettler Toledo pH meter was used for pH measurements throughout the study. Aqueous lead solutions ranging from 50 mg L^{-1} to 500 mg L^{-1} were studied to evaluate the effect of initial pollutant concentration on adsorption capacity. The effect of temperature on adsorption efficiency was analysed in the temperature range of 30-60°C. The equilibrium adsorption capacity ($q_{e,}$**mg** $\mathbf{g^{-1}}$**)** was calculated as

$$q_e = \frac{(C_0 - C_e)v}{m} \quad (1)$$

where C_0 and C_e are the initial and equilibrium concentration of Pb(II) ions in mg$\mathbf{L^{-1}}$, respectively. Here v is the volume of pollutant **(ml)** considered and m denoted the mass(**mg)** of the adsorbent taken (Chen et al., 2019). All experiments were carried out in triplicates and the mean values were considered.

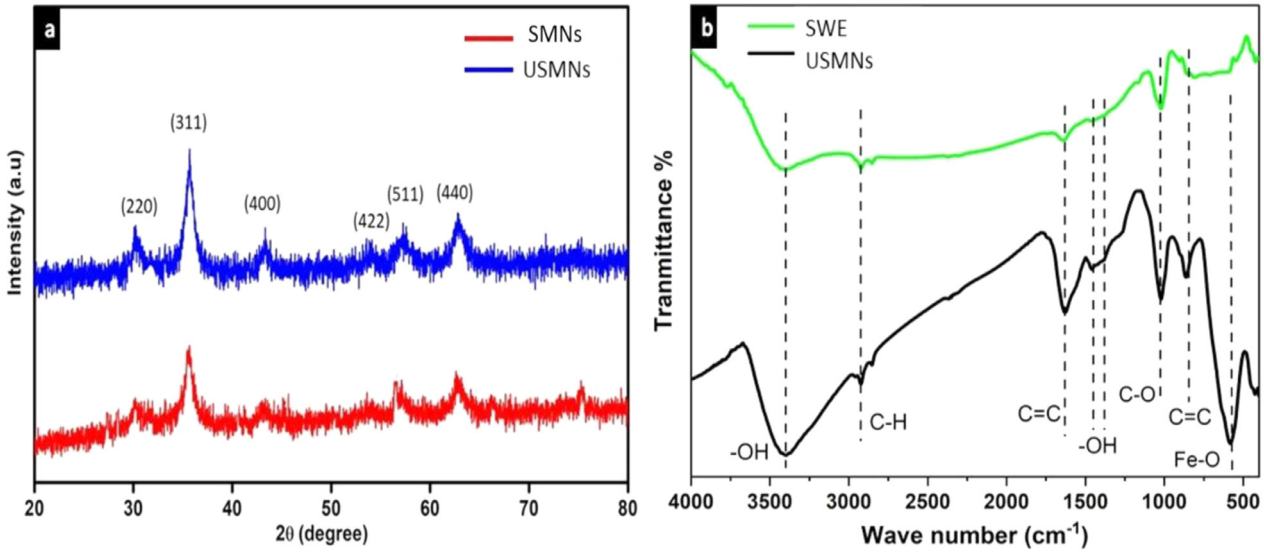

Fig. 1. (a) PXRD pattern of SMNs and USMNs (b) FTIR spectra of SWE and USMNs.

Though an adsorbent display superior adsorption capacity towards simulated target solution, the adsorption efficiency might get compromised when applied to real effluents due to the coexistence of different ions. The effect of different competing cations on the adsorption of Pb(II) by USMNs, owing to its superior performance, was investigated to ensure the unhindered efficacy of the adsorbent. The effluents for the study were simulated using equimolar solutions of Pb(II) and an additional cation. All other experimental constraints were kept optimal.

3. Results and discussion

3.1. Characterization of USMNs

The PXRD analysis confirmed the formation of inverse spinel magnetite nanoparticles. Fig. 1a depicts PXRD patterns of the formed USMNs and SMNs. All diffraction patterns of both USMNs and SMNs match well with the normal diffraction patterns of inverse spinel Fe_3O_4 and can be indexed to PDF no. 19–0629 (Cui et al., 2013). The width of the peaks depicts the ultrafine nature of the formed USMNs. Crystallite size was calculated using Scherrer's equation using the line broadening of the intense (311) diffraction plane using the equation

$$D = \frac{K\lambda}{\beta \cos\theta} \quad (2)$$

where D is the crystallite size, k is known as the Scherer's constant (K = 0.94) which denotes the shape of the particle, λ is the X-ray wavelength (1.54178 Å), β is full width at half maximum (FWHM) of the diffraction peak, and θ is the angle of diffraction (Holzwarth and Gibson, 2011). The Scherrer equation accounts for the broadening of the diffraction peaks solely due to crystallite size. The crystallite size was calculated to be ~6.1 nm and 16.2 nm for USMNs and SMNs, respectively. The computed lattice parameter of 8.39 and 8.37 Å for USMNs and SMNs, respectively, also correlates well with the reference file (de Carvalho et al., 2013). The evident difference in the crystallite size originated from the ultrasonic assistance in the case of USMNs. FTIR spectra of SWE and USMNs illustrated in Fig. 1b indicate the presence of several functional groups. The strong peak around 3435 cm^{-1} in SWE is attributed to hydroxyl groups from polyphenols. The peaks at 2927 cm^{-1} and 1630 cm^{-1} refer to C-H, and C=C, stretching vibrations, respectively while the peaks at 1378 cm^{-1} and 1058 cm^{-1} correspond to –OH and C-O bending vibrations of the plant metabolites (Ricci et al., 2015). The reoccurrence of the peaks along with a distinct peak at 575 cm^{-1} corresponding to the metal-oxygen vibrational band (Fe–O) at the tetrahedral site verifies the formation of magnetite conjugated with active phytochemical fragments derived from the extract (Wang et al., 2018).

The HR-TEM micrograph (Fig. 2a) exhibits nearly spherical and well-resolved monodisperse particles in the case of USMNs while SMNs (Fig. 2b) displayed larger particles and agglomerated morphology. This substantiates the effective surface refinement achieved through ultrasonic assistance and reduced magnetic dipolar interaction between particles. The estimated average particle diameter for USMNs and SMNs using the size distribution analysis was approximately 3.14 ± 0.25 nm and 11.03 ± 0.64 nm, respectively (Fig. 2c,d). the variation in size obtained from PXRD analysis is attributed to the capping of plant metabolites around the magnetite core. The interplanar spacing of approximately 0.18 nm observed for USMNs and 0.24 nm for SMNs concurs well with the lattice spacing of the (422) and (311) planes in crystalline Fe_3O_4. Moreover, the selected area electron diffraction (SAED) pattern of the USMNs and SMNs (Fig. 2e,f) in the selected area exhibits five distinguishable crystal planes of (440), (511), (400), (311), and (220) which agrees with the PXRD results (Rajan et al., 2020). It indicates that the precursor was fully converted to Fe_3O_4. The SAED pattern shows that the prepared sample is polycrystalline with a cubic inverse spinel crystal structure.

3.2. Mechanism of USMNs formation

Siam weed is a natural reservoir of polyphenols and flavonoids in addition to other active secondary metabolites. The plant is reported to contain complex mixtures of flavonoids and other phenolic compounds like salvigenin, sakuranetin, protocatechuic acid, p-hydroxy benzoic acid, ferulic acid, luteolin and vanillic acid. The aqueous flower extract also contains

3,5,4'-trihydroxy-7-methoxyflavanone, and 3,5,7-trihydroxy-4'-methoxyflavanon (Haji Jasnie, 2009). These phytochemicals have a variety of active sites like 6,7- di-hydroxy moieties, B-ring catechol, and 2,3 double bonds to strongly chelate with iron (Eze and Jayeoye, 2021). Primary phytoscreening of SWE revealed the presence of saponins, tannins, polyphenols, flavonoids, alkaloids, and glycosides in the aqueous extract. The total phenolic content (TPC) and total flavonoid content (TFC) were estimated to be 175.69 ± 1.21 mg GAE/g and 24.72 ± 0.87 (mg QE/g), respectively. The high amount of TPC and TFC approves

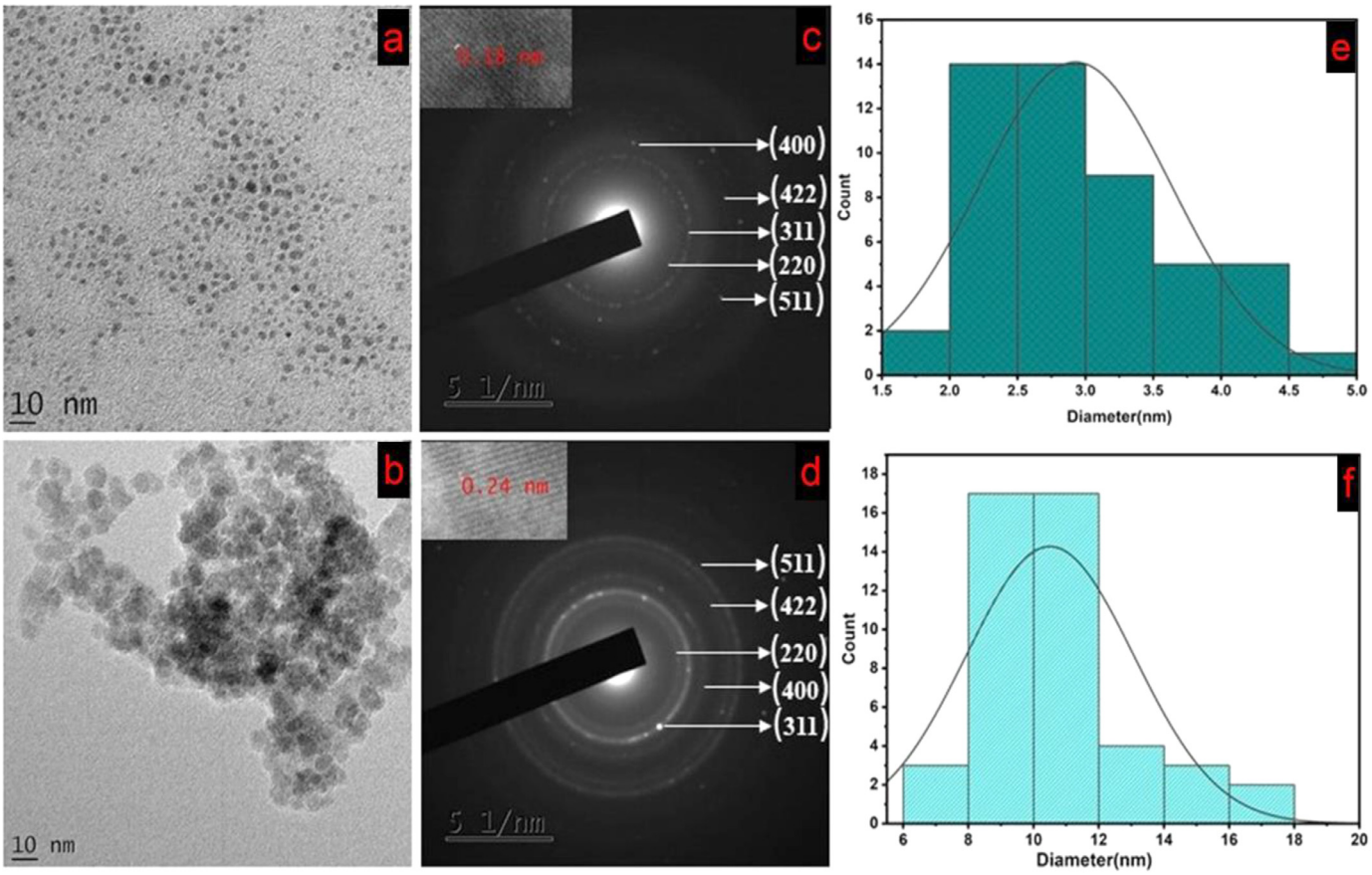

Fig. 2. HRTEM images of (a) USMNs (b) SMNs (c) SAED pattern of USMNs, (d) SAED pattern of SMNs (e) size distribution analysis of USMNs (f) size distribution analysis of SMNs

the effective extraction procedure adopted. The brown transparent SWE rapidly changed to dirty green precipitate upon the addition of $FeCl_3$ solution indicating the complexation of Fe^{3+} ions with polyphenols/flavonoids (Elhabiri et al., 2007). $NaHCO_3$ acts as neutralizing and electrostatic stabilizing agent in the reaction system enabling SWE to reduce Fe^{3+} ions as the hydrothermal treatment progresses. It is plausible that $NaHCO_3$ provides heterogeneous nucleating cores during the hydrothermal treatment. The local temperature gradient formed on the surface of the primary nanoparticles accelerates hydroxide to oxide conversion. The plant metabolites in the medium significantly reduce the collisions between the formed nuclei. As the frequency of collisions declines, the oriented attachment, and Ostwald ripening rate diminish, resulting in finer crystallite sizes. Surface reformations attained from the self-capping of phytometabolites prevented agglomeration and provided stability to the USMNs.

3.3. Adsorption batch experiments

The difference in the optimal contact time for Pb(II) ions removal by USMNs and SMNs is presented in Fig. 3. USMNs (1.5 gL^{-1}) displayed enhanced removal of Pb(II) ions (100 mgL^{-1}) in under 10 min whereas SMNs (1.5 gL^{-1}) took 20 min to attain 96.5% removal at inherent pH(5.7) and temperature. The increase in the optimal contact period for the adsorptive removal by SMNs is correlated to the agglomeration of nanoparticles and the increased particle size. The resultant reduction in the surface area decreases the adsorption efficiency of SMNs. The adsorption capacity of USMNs and SMNs were recorded at equilibrium as 66.43 and 64.32 mgg^{-1}, respectively at an initial concentration of 100 mgL^{-1} Pb(II).

3.4. Effect of pH and competing cations

It was observed that the pH of the medium controlled the efficiency of the adsorptive process. USMNs and SMNs displayed appreciable removal capacity at the pH range of 4–7. At and above pH 7 the adsorbate solution contained solid $Pb(OH)_2$. However, at pH values below 4 adsorption capacities dropped to 34.72 and 30.51 mg g^{-1} for USMNs and SMNs, respectively. Fig. 3b illustrates the change in Pb(II) equilibrium concentration with a change in pH for both adsorbents. The pH_{pzc} of the adsorbents was determined using the pH drift method to understand the surface electrostatic interactions of the adsorbent (Faria et al., 2004). Fig. 3c shows that at pH above 4 the surface of both the adsorbents are negative and can attract positively charged contaminants like lead ions onto it.

Industrial effluents are laden with several metal ions along with the target metal ion. The selectivity and efficiency of USMNs and SMNs towards Pb(II) removal were studied in the presence of metal ions including Cu^{+2}, Co^{+2}, Ni^{+2}, Hg^{+2}, and Cd^{+2} ions. The results of the study are compiled in Fig. 3d. It was confirmed that USMNs and SMNs exhibited selective and appreciable adsorption towards Pb(II) ions. The selective adsorptive removal is attributed to the combined effect of the size of hydrated ions and hydration energy. The metal ions with high free energy of hydration tend to remain in the aqueous phase reducing the possibility of interaction with the adsorbent surface. The free energy of hydration follows the order, $Ni^{+2} > Cu^{+2} > Hg^{+2} > Co^{+2} > Cd^{+2} > Pb^{2+}$ (Smith, 1977) .The lower free energy of hydration of Pb^{2+} ions, compared to the other divalent cation of choice, resulted in a lower hydrated radius, thereby enhancing the chances of reaching the adsorbent surface for adsorption (Cheng et al., 2012). Moreover, the larger ionic radius of

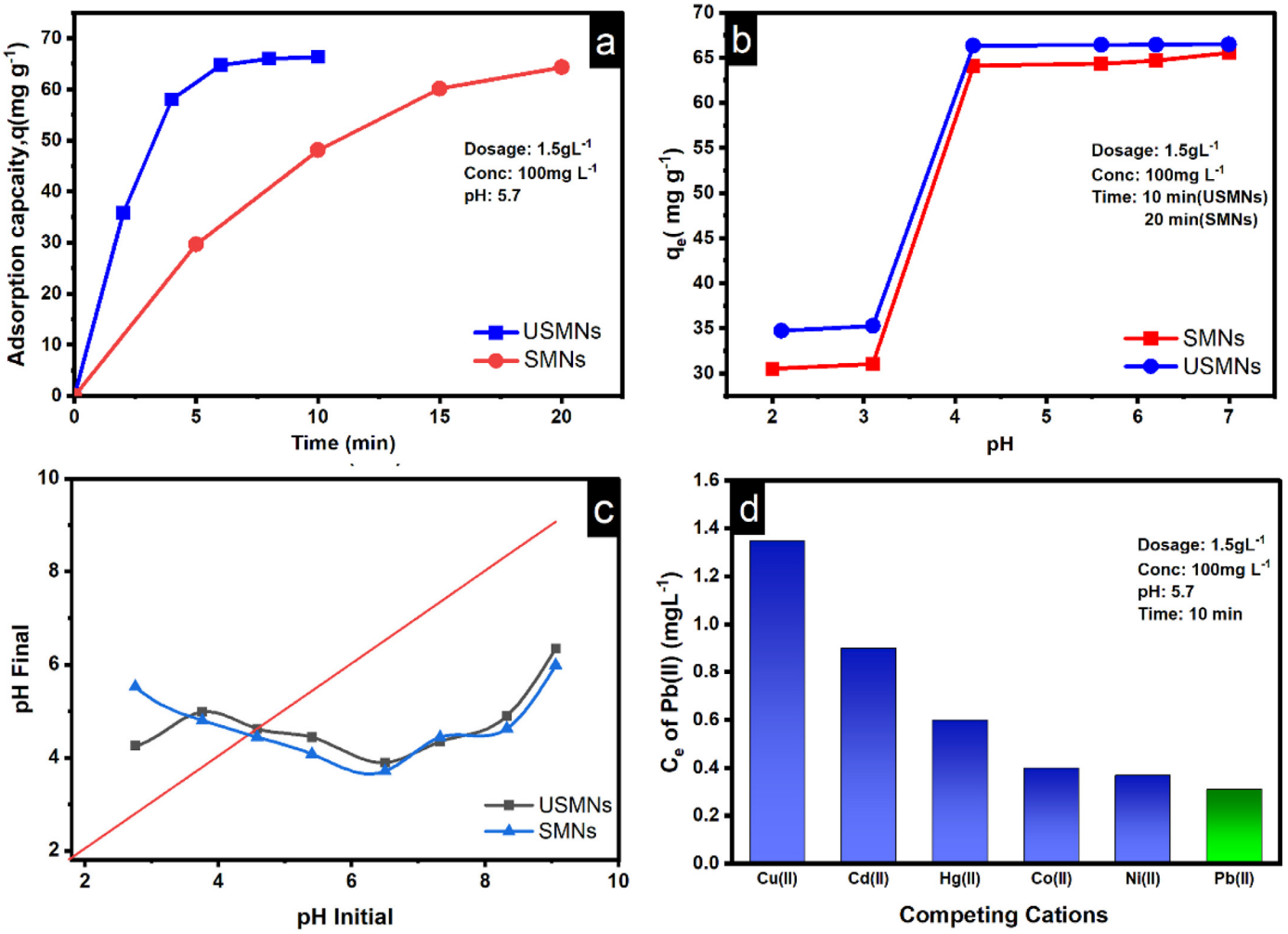

Fig. 3. (a) Adsorption Pb(II) on SMNS and USMNs (b) Effect of pH on adsorption (c) Surface charge analysis of USMNs (d) Selective adsorption of Pb(II) by USMNs in presence of competing cations.

Pb^{+2} ion makes it fit the active sites and facilitates binding to several surface groups simultaneously.

3.5. Adsorption equilibrium studies

The effect of the initial concentration of Pb(II) on the adsorption capacity of USMNs and SMNs was investigated to determine the maximum loading capacity of the adsorbents. Three adsorption isotherm models, (1) Langmuir, (2) Freundlich and (3) Temkin adsorption models were adopted for the Pb(II) adsorption equilibrium studies (Dada et al., 2012). Langmuir's model explains monolayer adsorption on a finite number of identical active sites. According to the Langmuir model, for homogenous systems,

$$q_e = \frac{q_m b C_e}{1 + bC_e} \tag{3}$$

where q_e is the amount of Cr(VI)/Pb(II) adsorbed at equilibrium, q_m is the maximum amount of Cr(VI) adsorbed per unit weight of the adsorbent (mg g^{-1}), C_e is the residual Pb(II) concentration and K_L is the Langmuir adsorption isotherm constant. The linear form of the equation is given by

$$\frac{C_e}{q_e} = \frac{1}{q_m K_L} + \frac{C_e}{q_m} \tag{4}$$

The Freundlich model can account for multilayer and non-equivalent adsorption sites and is given by the equation,

$$q_e = K_F C_e^{1/n} \tag{5}$$

Where K_F and n are Freundlich adsorption isotherm constants and n is the measure of the heterogeneity of the system. The linearized equation is expressed as,

$$\ln q_e = \ln K_F + \frac{1}{n} \ln C_e \tag{6}$$

Temkin adsorption isotherm equation, which considers both monolayer and multilayer adsorption, is given as

$$q_e = \frac{RT}{B_T} \ln K_T C_e \tag{7}$$

where B_T is the Temkin isotherm constant and K_T is the Temkin isotherm equilibrium binding constant. The linearized form is given below,

$$q_e = B_T \ln K_T + B_T \ln C_e \tag{8}$$

The obtained plots are presented in Fig. 4. The model with an R^2 value close to one and predicts q_m comparable to the experimental adsorption capacity was considered the best fit. Both USMNs and SMNs followed the Langmuir model of adsorption (Fig. 4b). This indicates monolayer coverage of the adsorbate on a homogeneous surface of the adsorbent, where all the active sites maintain equivalent energies. It also suggests negligible interaction between adsorbed moieties

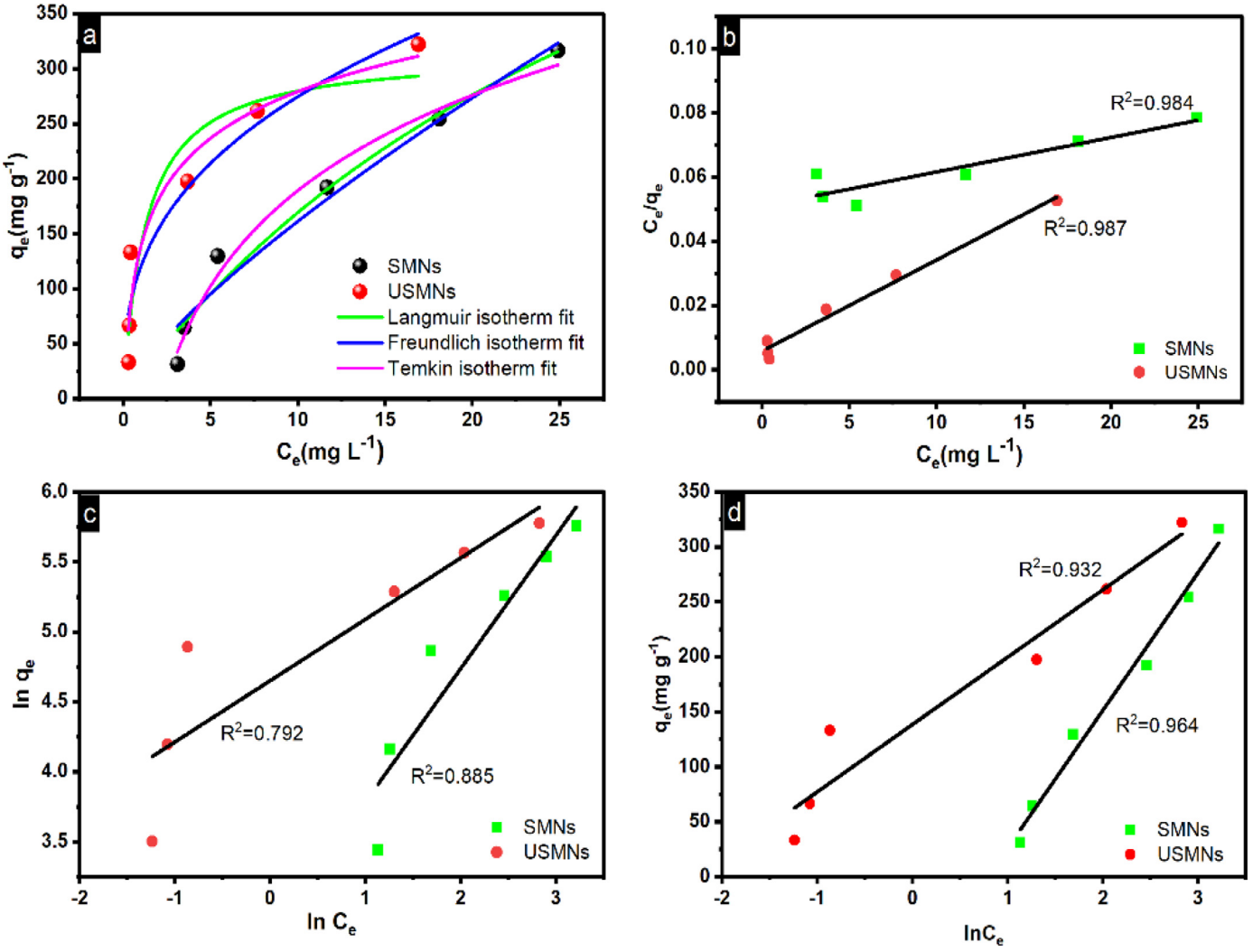

Fig. 4. (a) Nonlinear adsorption isotherm fit for Pb(II) adsorption on SMNS and USMNs, the linear fit of (b) Langmuir isotherm (c) Freundlich isotherm (d) Temkin isotherm

(Maiti et al., 2017). The dimensionless separation factor R_L is a measure of the affinity between the adsorbent and adsorbate, given by the equation

$$R_L = \frac{1}{1 + bC_0} \tag{9}$$

where C_0 is the highest initial adsorbate concentration. Generally, for favorable adsorption R_L ranges between 0 to 1, and for unfavorable adsorption $R_L > 1$ or $R_L = 1$. The values obtained for adsorption of Pb(II) on SMNs and USMNs were 0.064 and 0.0025, respectively. From the obtained R_L value a favorable parameter K_{C0} was derived.

$$K_{C_0} = \frac{1}{R_L} - 1 \tag{10}$$

The adsorption is considered favorable when the K_{C0} value is between 1 and 10. K_{C0} values higher than 10 denote spontaneous and highly probable adsorption (Joshy et al., 2021). The calculated value of K_{C0} for SMNs and USMNs is 14.625 and 394.25, respectively. The parameters derived from the Langmuir adsorption indicated the highly favorable nature of the adsorption of the target metal ion on prepared magnetite nanoparticles. Table 1 summarises the adsorption isotherm modelling equations used, and the results obtained from the study. The details of the adsorption batch experiments using different initial concentrations of Pb(II) solutions are listed in Table S1.

3.6. Adsorption kinetics and thermodynamics

Adsorption kinetic modelling reflects the relationship between adsorption capacity and contact time. The Pb(II) removal occurred at the highest rate for the first 4 and 15 min for USMNs and SMNs, respectively, owing to the high concentration gradient on the solid-liquid interface in the beginning. Pseudo first order, pseudo second order, and Elovich models (Simonin, 2016; Günay et al., 2007) were simulated to fit the experimental data to examine the kinetic parameters of Pb(II) adsorption (Fig. 5). Pseudo first order kinetics is generally used in the form,

$$q_t = q_e\left(1 - e^{-k_1 t}\right) \tag{11}$$

Where q_t is the adsorption capacity at time t, q_e is the equilibrium adsorption capacity and k_1 is the pseudo first order rate constant. It is generally used to explain the adsorption process during the initial stage. The linearized equation is expressed as,

$$log\ (q_e - q_t) = logq_e - \frac{k_1 t}{2.303} \tag{12}$$

The commonly used form of pseudo second order is given below,

$$q_t = \frac{q_e^2 k_2 t}{1 + q_e k_2 t} \tag{13}$$

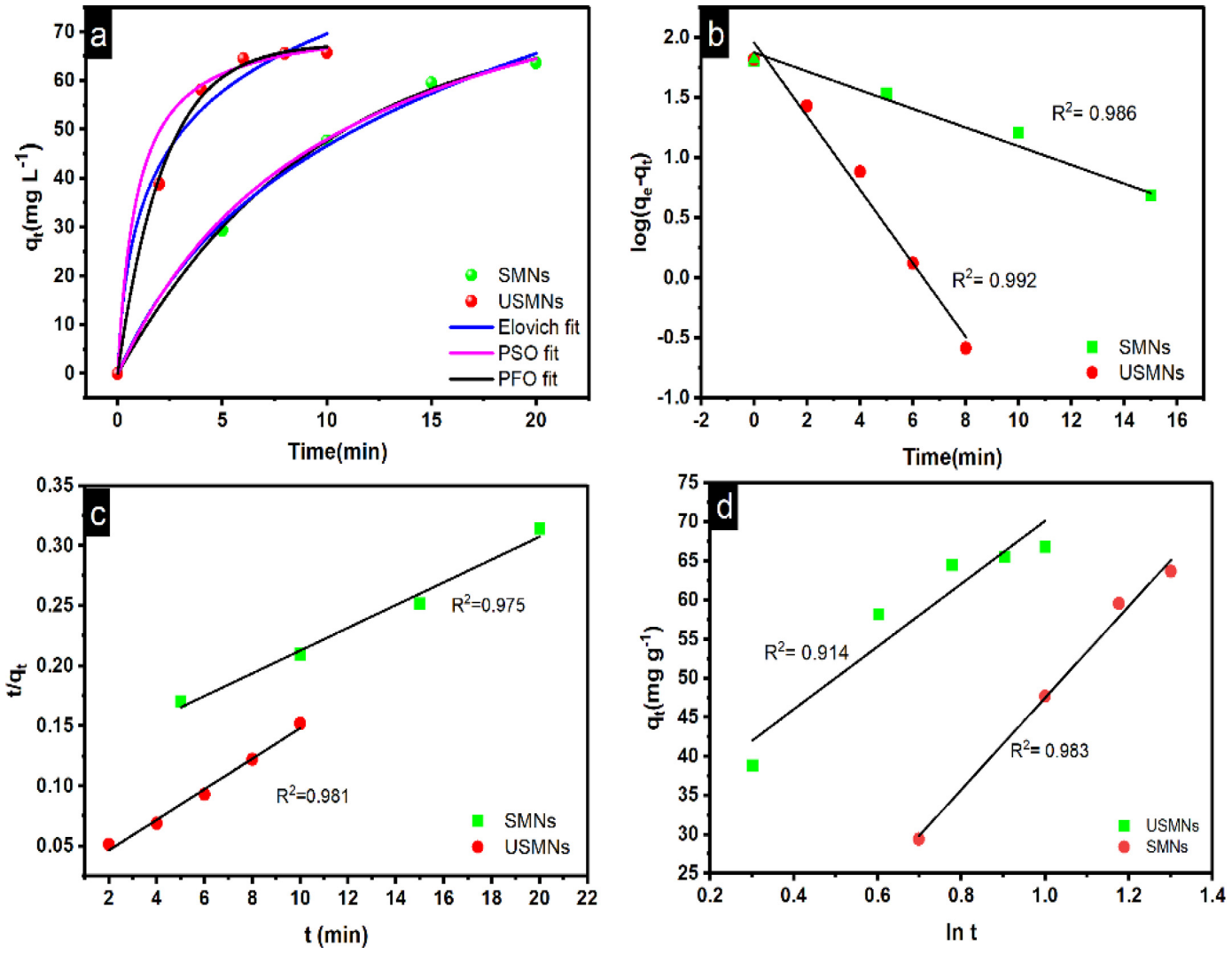

Fig. 5. (a) Nonlinear fit of different kinetic models for SMNs and USMNs, linear fit of (b) pseudo first order, (c) pseudo second order, (d) Elovich model.

Here, k_2 represents the pseudo second order rate constant. The model can be linearized as,

$$\frac{t}{q_t} = \frac{1}{k_2 q_e^2} + \frac{t}{q_e} \tag{14}$$

Elovich kinetics is another frequently used model to collect information about the kinetics of adsorption. The equation is given as below,

$$q_t = \frac{1}{b} ln(1 + abt) \tag{15}$$

a and b represent the initial rate of adsorption and the extent of surface coverage, respectively. The model is represented in linear form as,

$$q_t = \frac{1}{b} ln(ab) + \frac{1}{b} ln(t) \tag{16}$$

The conforming fit was determined by the R^2 value and closeness of the predicted equilibrium adsorption capacity to the experimental value. It was found that the removal of Pb(II) by USMNs and SMNs is compliant with the pseudo-first-order model similar to few recent reports (Günay et al., 2007; Lagergren, 1898; Forghani et al., 2020). It indicates that the adsorption occurs through diffusion through the interface. The details of the derived parameters are tabulated in Table 1.

The effect of temperature on the adsorption process was studied by performing adsorption experiments at selected temperatures. Batch thermodynamic experiments were studied between 303 and 333K, for both SMNS and USMNs. Thermodynamic parameters were computed using the Eqs. (17)–(19) given below.

$$K_d = \frac{q_e}{C_e} \tag{17}$$

$$lnK_d = \frac{-\Delta H}{RT} + \frac{\Delta S}{R} \tag{18}$$

$$\Delta G = \Delta H - T\Delta S \tag{19}$$

Here, K_d represents the equilibrium constant. Fig. 6 shows the simulated plot of ln K_d v/s 1/T for adsorption of Pb(II) ions on SMNS and USMNs at different temperatures. Table 2 outlines the obtained thermodynamic parameters. e positive ΔH value indicated the endothermic nature of the adsorption. The positive ΔS values suggested the rising disorder at the interface during the adsorption of Pb(II) ions onto the magnetite nanoparticles. The high negative values of ΔG indicated the spontaneity of the process.

3.7. Regeneration and recyclability

The exhausted adsorbents were recovered using 0.1 M HCl at room temperature in both cases. The sudden change in pH of the system triggered electrostatic charge reversal on the adsorbent surface resulting in

Table 1
Results from adsorption isotherm and kinetic modeling studies on adsorption of Pb(II) by SMNs and USMNs.

	Models	Parameters	
		SMNs	**USMNs**
Isotherms	*Langmuir Isotherm*	q_m(mg g^{-1}) = 305.57 K_L = 0.029 R^2 = 0.979	q_m(mg g^{-1}) = 315.43 K_L = 0.787 R^2 = 0.988
	Freundlich Isotherm	K_F = 34.93 N = 0.761 R^2 = 0.915	K_F = 120.12 n = 0.359 R^2 = 0.955
	Temkin Isotherm	K_T (Lg^{-1}) = 12.58 B($Jmol^{-1}$) = 61.25 R^2 = 0.946	K_T (Lg^{-1}) = 7.43 B($Jmol^{-1}$) = 120.18 R^2 = 0.983
Kinetics	*Pseudo first order*	q_e (mg g^{-1}) = 73.69 k_1(h^{-1}) = 0.104 R^2 = 0.998	q_e (mg g^{-1}) = 67.66 k_1(h^{-1}) = 0.454 R^2 = 0.997
	Pseudo second order	q_e (mg g^{-1}) = 98.92 k_2(g (mg $h)^{-1}$) = 9.62E-4 R^2 = 0.993	q_e (mg g^{-1}) = 72.79 k_2(g (mg $h)^{-1}$) = 0.0148 R^2 = 0.995
	Elovich	a (mg g^{-1}) = 10.04 b = 0.029 R^2 = 0.994	a (mg g^{-1}) = 90.67 b = 0.056 R^2 = 0.973

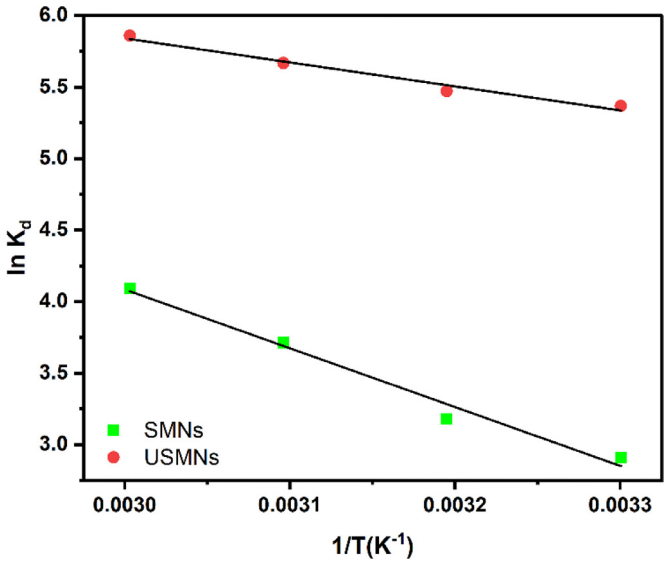

Fig. 6. Thermodynamic study on adsorption of Pb(II) on SMNs and USMNs.

the desorption of the pollutant. The adsorbents were then washed using ethanol followed by distilled water. Both adsorbents were dried at 60°C to regenerate the pure adsorbents. The efficiency of USMNs and SMNs for five consecutive adsorption-desorption cycles is illustrated in Fig. 7. The loss of adsorbent mass during recycling was minimal due to the easy and effective magnetic separation. Regenerated adsorbents displayed sustained adsorption capacities throughout the cycles. The invariable adsorption capacity demonstrates the effectiveness of the adapted regeneration method and the high stabilization derived from phytochemical capping. AAS analysis confirmed the absence of leached iron during the adsorption, desorption and elution cycles. It is presumed that the phytoconjugate capping derived from strong phenolic chelation provides protection to the magnetite core of the adsorbents during the elution process. However, it was observed that further increase in the acid concentration accelerated the desorption but triggered the leaching of iron, which was evident from the brown colour of the desorbed

Table 2
Thermodynamic parameters of adsorption of Pb(II) onto SMNs and USMNs.

	Temperature (K)	ΔG (kJ mol^{-1} K^{-1})	ΔH(kJ mol^{-1} K^{-1})	ΔS ($Jmol^{-1}$ K^{-1})
SMNs	303	-13.44	13.949	90.39
	313	-14.35		
	323	-15.24		
	333	-16.15		
USMNs	303	-7.167	34.147	136.356
	313	-8.532		
	323	-9.895		
	333	-11.26		

solution. A comparative list of recent reports (Lingamdinne et al., 2017; Lingamdinne et al., 2020; Fayazi et al., 2019; Jiang et al., 2015; Ali et al., 2019) on biogenic iron oxide adsorbents for lead removal is presented in Table 3.

3.8. Effect of Pb(II) adsorption on magnetic properties

The coalescence of other metal ions on iron oxide nanoparticles can trigger changes in their magnetic properties. Magnetic adsorbents that remove heavy metal ions are vulnerable to such obvious transformations, but these changes are seldom investigated. The effect of the adsorption of lead on the magnetic properties of USMNs and SMNs was inspected using VSM analysis. The absence of a hysteresis loop, zero coercivity, and zero remnant magnetization at room temperature revealed the superparamagnetic nature of the adsorbents. The saturation magnetization values (M_s) for SMNS and USMNs were 46.83 and 38.53 emug[1], respectively. The small M_s compared to the bulk magnetite particles, is the result of surface capping provided by the plant metabolites and the effective size reduction attained through the novel synthesis route. The slightly high value of M_s for SMNs is a consequence of a comparatively large magnetite core. The interactions with diamagnetic materials attenuate the inherent magnetic properties of a material. Here, the adsorption of Pb(II) caused a drastic decrease in the saturation magnetization value as evident from Fig. 8. The M_s for Pb-loaded adsorbents were recorded as 32.95 and 22.42 $emug^{-1}$ for Pb-SMNs and Pb-USMNs, respectively. The adsorbed layer of diamagnetic lead moieties on the magnetite surface reduces the magnetic moment of both adsorbents without interfering with the superparamagnetic nature of the adsorbents. It was noted that despite the reduction in the M_s value, an external magnet could effectively separate the exhausted adsorbent from the analyte.

3.9. Mechanism of adsorption

Surface charge studies on USMNs reveal the prevalence of a negative surface above pH 4. The inherent pH of the simulated Pb(II) effluent was 5.7. The lead species detected to dominate in solution at this pH is primarily Pb^{2+}ions (Giraldo and Moreno-Piraján, 2008). This triggers an electrostatic interaction between the adsorbent and positively charge lead species in the medium, initiating the adsorption process. Owing to the displayed superior adsorption characteristics, USMNs were further analysed using the FTIR, XRD, XPS and FESEM techniques for comprehending the adsorption mechanism of magnetite nanoparticles and speciation of lead on the adsorbent surface. No visible changes were observed in FTIR and XRD plots of Pb-loaded adsorbents. XPS data was acquired at room temperature using a monochromatic mg Kα X-ray source (1253.6 eV) and at a background pressure of 2×10^{-8} mbar. XPS profiling of USMNs confirmed the presence of Fe, O, C and Fe, O, C, Pb before and after adsorption, respectively. C 1s peak at 284.6 eV was used for binding energy calibration. The fitted core-level spectra of each element after a Shirley background subtraction in the concerned range are given in Fig. 9. The Fe 2p core-level spectrum of USMNs displayed two peaks corresponding to Fe $2p_{3/2}$ and Fe $2p_{1/2}$ at ~710.8 eV and ~724.1 eV, respectively, verifying the magnetite phase. The fitted Fe 2p

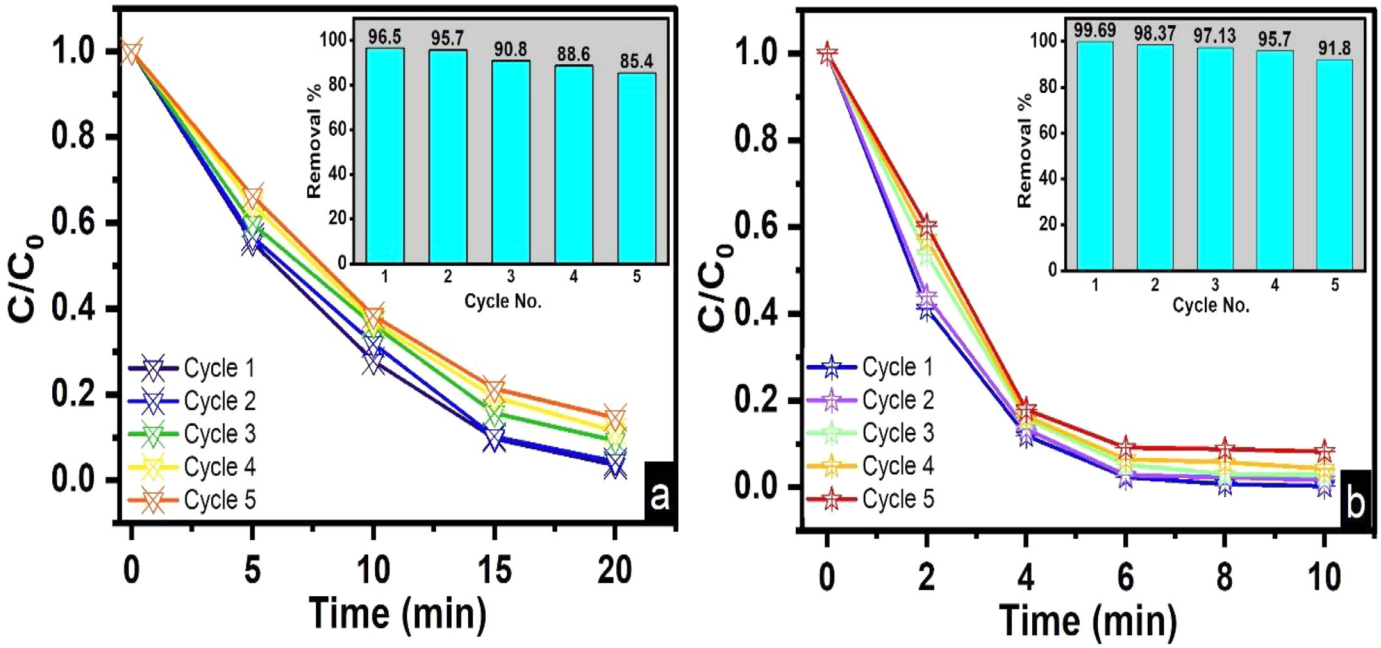

Fig. 7. Recyclability of (a) SMNs and (b) USMNs.

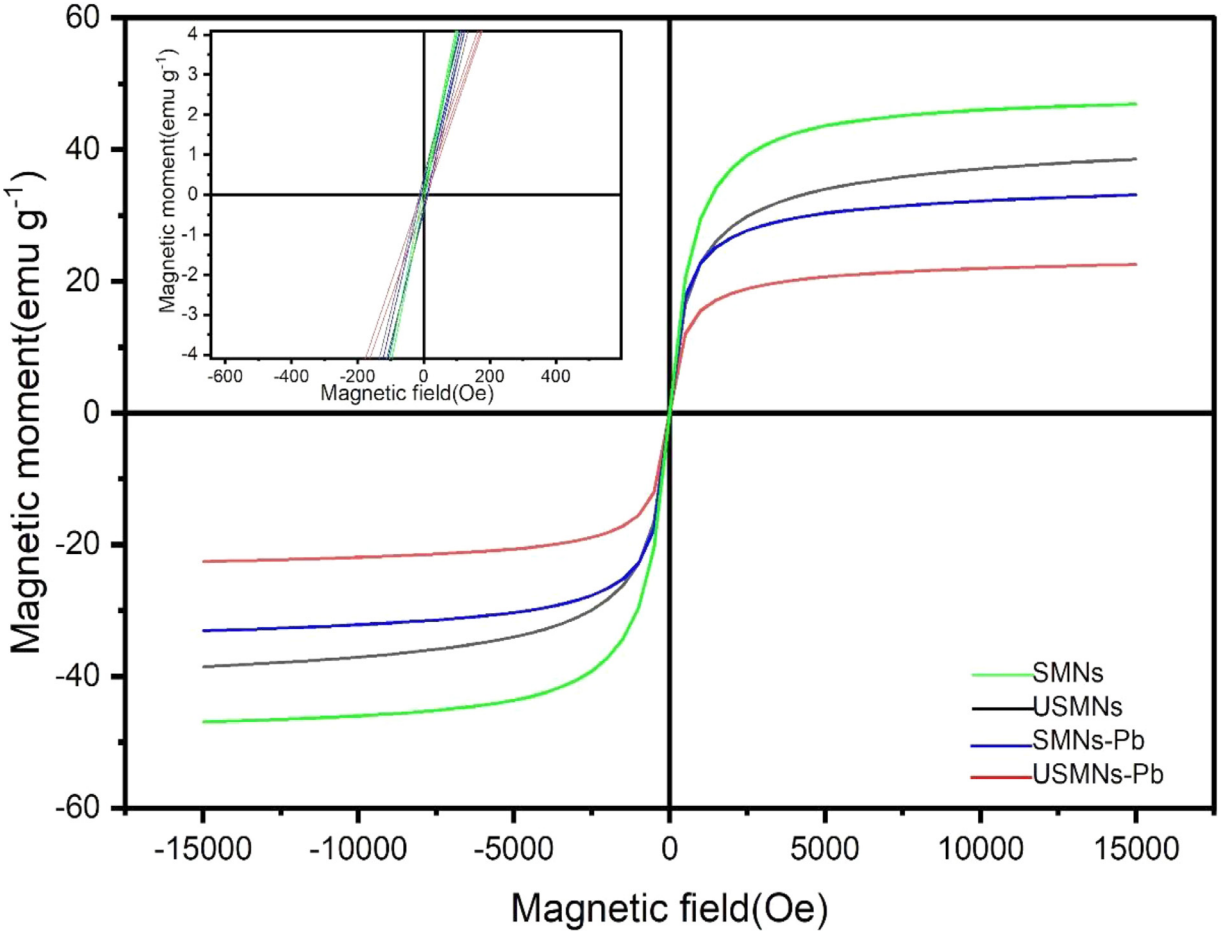

Fig. 8. Magnetic characterization of the adsorbents pre and post-adsorption of Pb(II); inset showing close-up image of the **center of the plot.**

Table 3
List of recent reports of biogenic iron oxide-based adsorbents for Pb(II) removal.

Adsorbent	Synthesis route of iron oxide	Adsorbent dosage	pH	Optimum contact period (min)	q_m(mg g^{-1})	Refs.
T-Fe_3O_4	Tangerine peel mediated	0.625 gL^{-1}	4.5	95	100	Lingamdinne et al. (2017)
MISFNPs	CLC seed extract	0.5 gL^{-1}	4	100	67.5	Lingamdinne et al. (2020)
Sep-Fe-MnO_2	Hydrothermal	0.04 mg	6	60	131.58	Fayazi et al. (2019)
MLP	Litchi peel derived	5 gL^{-1}	6	120	78.74	Jiang et al. (2015)
3-MPA@PMNPs	*F. chinensis Roxb* leaf extract	0.5 gL^{-1}	6.5	60	68.41	Ali et al. (2019)
SMNs	Siam weed flower extract	1.5 gL^{-1}	5.7	10	305. 57	Present work
USMNs	Siam weed flower extract	1.5 gL^{-1}	5.7	10	315.43	Present work

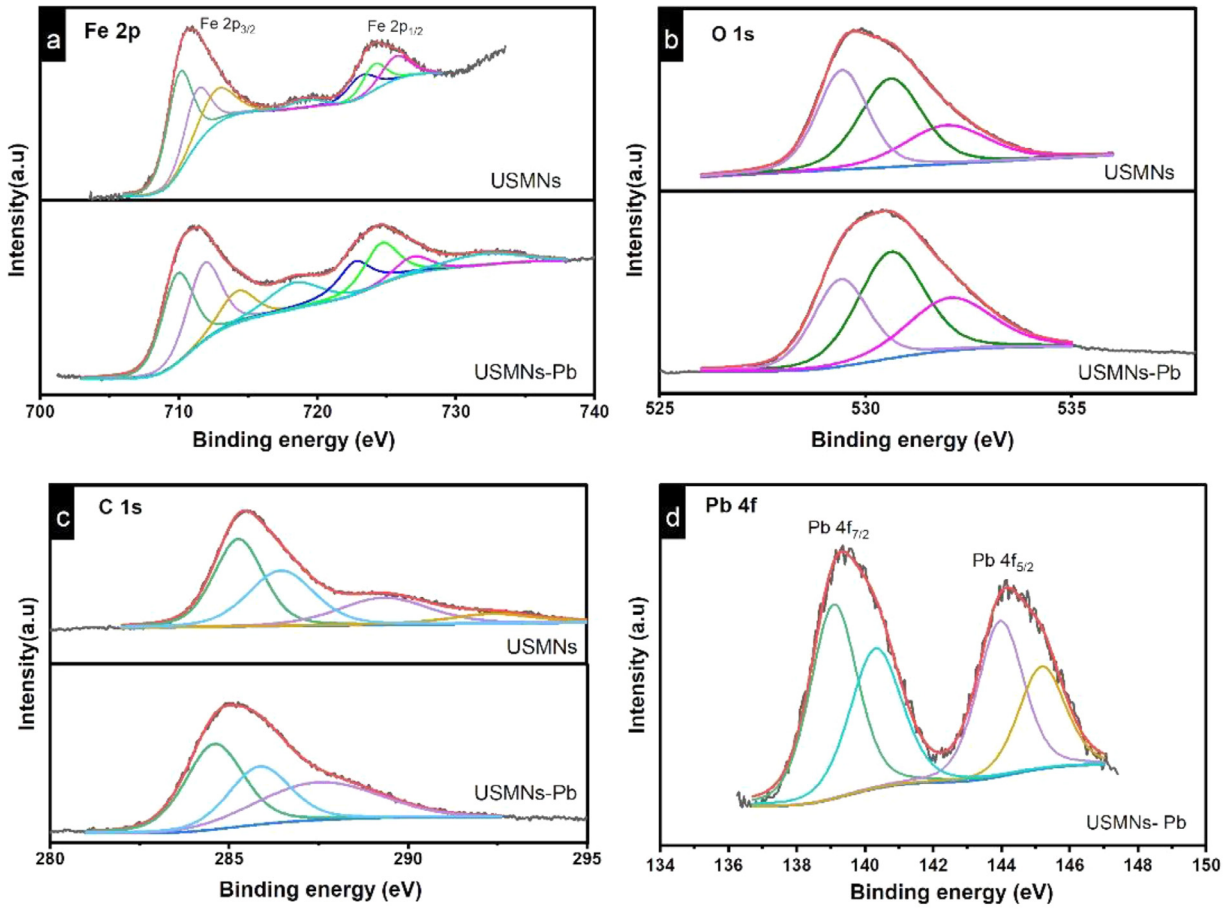

Fig. 9. Pre and post adsorption XPS profile of USMNs for (a) Fe 2p (b) O 1s (c) C 1s and (d) Pb 4f core levels.

spectrum (Fig. 9**a)** consists of peaks at 710.1, 711.3, 712.8, 723.1,724.1 and 725.6 eV. The peaks at 710.1and 723.1 eV correspond to the Fe^{2+} species in the octahedral (Oh) site. The peaks representing Fe^{3+} species in the octahedral site were found at a binding energy of 711.3 and 724.1 eV. The peak at 712.8 and 725.6 eV corresponds to Fe^{3+} in tetrahedral sites. The vacancy cascade peak which is a common occurrence in iron oxide species is spotted at ~719.1 eV (Poulin et al., 2010). A slight chemical shift to the higher binding energy and higher FWHM for all the observed peaks from that of the pure magnetite is correlated to the capping and stabilization of USMNs by plant metabolites. The O 1s core-level spectrum (Fig. 9**b**) exhibits peaks at ~529.4 eV and 530.6 eV correlated to Fe-O and surface OH moieties, respectively. The peak with higher binding energy at 531.9 eV is attributed to polyphenolic hydroxyl groups adhered to USMNs (McCafferty and Wightman, 1998). The C 1s profile of USMNs (Fig. 9**c**) was fitted into four components with binding energies ~284.6, 286.5, 289.3, and 290.1 eV corresponding to C-C, C-O, C=O, and π-π interactions, respectively (Mathew et al., 2020).

The XPS spectra of exhausted adsorbent (USMNs-Pb) revealed the presence of Pb(II) species on the surface. Peak fitted Pb 4f spectra exposed the presence of two different Pb(II) moieties on the surface(Fig. 9**d**). Accordingly, the peaks at 139.1 and 143.9 eV were assigned to Pb-O bonds whereas the peaks at 140.3 and 145.1 eV represent Pb interacting with the hydroxyl groups (Thomas and Tricker, 1975). The peak at 530.6 eV in O 1s core spectra displayed an increase in intensity owing to the increase in the total number of metal-OH bonds formed on the surface. The association of Pb(II) on the surface produced slight chemical shifts in Fe 2p and C 1s spectra of USMNs-Pb towards higher binding energy values. The Fe 2p vacancy cascade peaks are more prominent in USMNs-Pb owing to the variations that occurred at the surface after adsorption. The changes in the C 1s spectra may be attributed to the involvement of π electrons in the adsorption process. Further experimental and analytical studies are required for further understanding of the role of phytochemical fragments during the adsorptive removal of lead. The fitting parameters obtained are summarised in **Table S2.**

The FESEM images USMNs before and after adsorption are displayed in Fig. 10. The FESEM images of USMNs illustrate a unique morphology of an assembly of tiny nanobuds resembling a 'broccoli head'. The size of these nanobuds range from 30 to 70 nm. There are numerous inter-

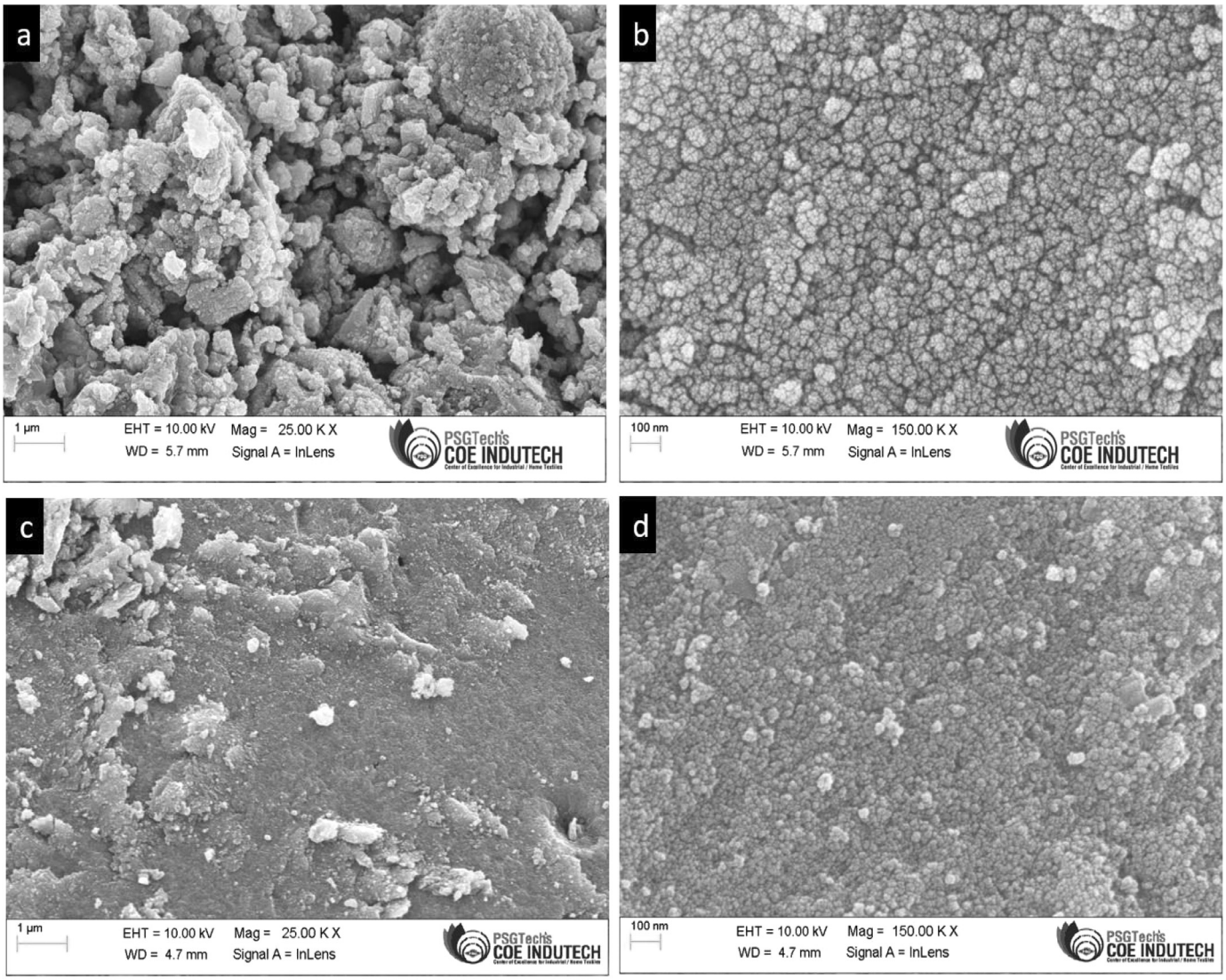

Fig. 10. FESEM micrographs of (a & b) USMNs and (c & d) Pb-loaded USMNs.

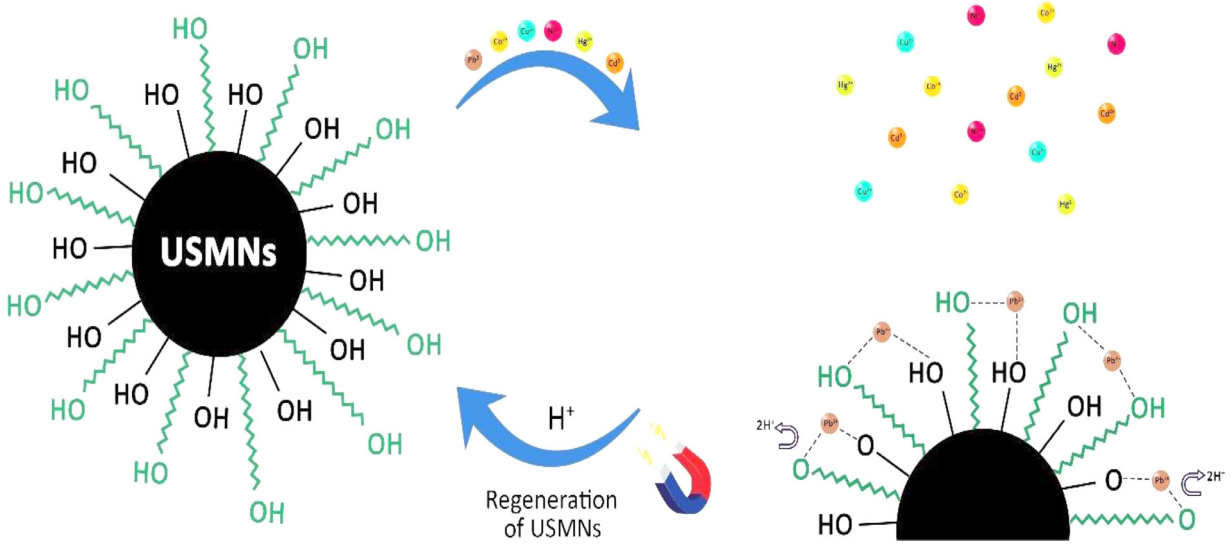

Fig. 11. Schematic representation of proposed mechanism for selective Pb(II) removal by USMNs.

linked void interstices of average width of ~17 nm, surrounding each cluster of nanobuds (Fig. S1). These interstices act as interlinking channels that facilitate the easy transport and anchoring of Pb(II) species on the adsorbent surface. Prominent changes were visible on USMNs' surface upon adsorption of lead moieties. More protruding clusters appeared on the surface and the void interstices were filled with deposition of lead species. EDAX spectra of USMNs (Fig. S2) revealed the presence of Fe, C, and O confirming the phytoconjugation on the iron oxide surface. Whereas EDAX analysis of Pb-loaded USMNs displayed the presence of Pb and negligible changes in the composition of other elements.

The results discussed above speculate that the removal of Pb(II) by USMNs primarily involves the following attributes. (1) Physical adsorption: the possible enhancement of surface area achieved through appreciable reduction of particle size instigates adsorption of the target metal ions onto USMNs. FESEM and XRD results post adsorption validate an amorphous deposition of lead species on the USMNs' surface. (2) Electrostatic interactions: the strong electrostatic interactions between the negatively charged adsorbent surface and the cationic lead species further promote the adsorptive removal of lead by USMNs. (3) Interfacial interactions: the adsorption proceeds through the interactions of the surface hydroxyl groups of USMNs with Pb^{2+} ions. Elimination of a fraction of H^{+} ions by Pb^{2+} resembling an ion exchange process subsequently gives rise to two different lead species on the adsorbent surface. A schematic representation of the proposed mechanism is given in Fig. 11.

4. Conclusion

In this work, a facile one-pot strategy was developed for the synthesis of superparamagnetic ultrasmall magnetite nanoparticles by using siam weed flower extracts for the first time. The synthesized nanoparticles were characterized using assorted instrumental techniques including XRD, FTIR, HRTEM, VSM, and XPS. The reasonable reduction in size and the monodispersity attained through ultrasonic homogenization is evident in the TEM micrographs. The negative charge prevailing on the surface of the nanoparticles made it capable of adsorbing the target metal ion Pb(II). Moreover, the self-capping of the plant metabolites on USMNs increased the number of active sites for the target metal to bind. At the inherent pH of the simulated effluent, the adsorption capacity of USMNs reached 66.43 mg g^{-1} for 100 mg L^{-1} Pb(II) solution in under 10 min. USMNs exhibited superior adsorptive properties owing to the enhanced surface area achieved through size reduction. The surface hydroxyls present on the USMNs play a crucial role in binding the Pb^{+2} ions further accelerating the adsorptive removal. The adsorption equilibrium and adsorption kinetics conformed well to the Langmuir adsorption isotherm model and pseudo first order kinetics model, respectively. The selectivity of the USMNs towards Pb(II) can aid in the recovery of the metal ion from effluent mixtures in practical scenarios. The adsorbents were regenerated and used to confirm their economic viability. Though the magnetic moment of the adsorbents declined after the adsorption, the remnant saturation magnetization was enough to attain facile magnetic separation of the adsorbents. The results of the study indicate the potential of USMNs as efficient, selective, and recyclable magnetic adsorbents for aqueous Pb(II). Furthermore, the economic and greener synthesis route that might serve as an effective weed control upon scaling up makes USMNs more promising Eqs. (1)–(16).

Funding information

I am to submit herewith the research paper entitled 'Weed to nanoseeds: Ultrasonic assisted one-pot fabrication of superparamagnetic magnetite nano adsorbents from Siam weed flower extract for the removal of lead from water' for your kind consideration to be published in the prestigious journal, Journal of Hazardous Materials Advances. No external funding is received for this project from any of the funding agencies in and out of the country other than the facilities provided by the department of Chemistry, University of Calicut.

Declaration of Competing Interest

The authors declare that they have no known competing financial interests or personal relationships that could have appeared to influence the work reported in this paper.

Data availability

Data will be made available on request.

Acknowledgments

The author acknowledges the support provided by Dr. Pradeep A.K, Department of Botany, University of Calicut in identifying the collected plant. Facility and technical help for AAS measurements were provided by Dr. C.C Harilal and Dr. Ajayan K.V, Department of Botany, University of Calicut. The research was supported by technical assistance from CSIF-University of Calicut, INUP CeNSE-IISc, Bangalore, SAIF- IIT Madras, STIC-CUSAT Kerala, DST-FIST Facility, Department of Chemistry, University of Calicut and KSCSTE Facility at CCS, Department of Chemistry, University of Calicut. One of the authors (JG)is thankful to CSIR-HRDG, Govt. of India for providing Senior Research Fellowship.

Supplementary materials

Supplementary material associated with this article can be found, in the online version, at doi:10.1016/j.hazadv.2022.100163.

References

Aigbedion-Atalor, P.O., Day, M.D., Idemudia, I., Wilson, D.D., Paterson, I.D., 2019. With or without you: stem-galling of a tephritid fly reduces the vegetative and reproductive performance of the invasive plant Chromolaena odorata (Asteraceae) both alone and in combination with another agent. BioControl 64 (1), 103–114.

Ainsworth, E.A., Gillespie, K.M., 2007. Estimation of total phenolic content and other oxidation substrates in plant tissues using Folin–Ciocalteu reagent. Nat. Protoc. 2 (4), 875–877.

Ali, A., Hira Zafar, M.Z., ul Haq, I., Phull, A.R., Ali, J.S., Hussain, A., 2016. Synthesis, characterization, applications, and challenges of iron oxide nanoparticles. Nanotechnol. Sci. Appl. 9, 49.

Ali, I., Peng, C., Naz, I., 2019. Removal of lead and cadmium ions by single and binary systems using phytogenic magnetic nanoparticles functionalized by 3-marcaptopropanic acid. Chin. J. Chem. Eng. 27 (4), 949–964.

Ali, I., Peng, C., Naz, I., Khan, Z.M., Sultan, M., Islam, T., Abbasi, I.A., 2017. Phytogenic magnetic nanoparticles for wastewater treatment: a review. RSC Adv. 7 (64), 40158–40178.

Bibi, I., Nazar, N., Ata, S., Sultan, M., Ali, A., Abbas, A., Jilani, K., Kamal, S., Sarim, F.M., Khan, M.I., 2019. Green synthesis of iron oxide nanoparticles using pomegranate seeds extract and photocatalytic activity evaluation for the degradation of textile dye. J. Mater. Res. Technol. 8 (6), 6115–6124.

Bolisetty, S., Peydayesh, M., Mezzenga, R., 2019. Sustainable technologies for water purification from heavy metals: review and analysis. Chem. Soc. Rev. 48 (2), 463–487.

Chen, W., Lu, Z., Xiao, B., Gu, P., Yao, W., Xing, J., Asiri, A.M., Alamry, K.A., Wang, X., Wang, S., 2019. Enhanced removal of lead ions from aqueous solution by iron oxide nanomaterials with cobalt and nickel doping. J. Clean. Prod. 211, 1250–1258.

Cheng, T., Lee, M., Ko, M., Ueng, T., Yang, S., 2012. The heavy metal adsorption characteristics on metakaolin-based geopolymer. Appl. Clay Sci. 56, 90–96.

Cui, H., Liu, Y., Ren, W., 2013. Structure switch between α-Fe_2O_3, γ-Fe_2O_3 and Fe_3O_4 during the large scale and low temperature sol–gel synthesis of nearly monodispersed iron oxide nanoparticles. Adv. Powder Technol. 24 (1), 93–97.

Cuthbert, R.N., Diagne, C., Haubrock, P.J., Turbelin, A.J., Courchamp, F., 2022. Are the "100 of the world's worst" invasive species also the costliest? Biol. Invasions 24 (7), 1895–1904.

Dada, A., Olalekan, A., Olatunya, A., Dada, O., Langmuir, Freundlich, 2012. Temkin and Dubinin–Radushkevich isotherms studies of equilibrium sorption of Zn2+ unto phosphoric acid modified rice husk. IOSR J. Appl. Chem. 3 (1), 38–45.

de Carvalho, J.F., de Medeiros, S.N., Morales, M.A., Dantas, A.L., Carriço, A.S., 2013. Synthesis of magnetite nanoparticles by high energy ball milling. Appl. Surf. Sci. 275, 84–87.

Elhabiri, M., Carrër, C., Marmolle, F., Traboulsi, H., 2007. Complexation of iron(III) by catecholate-type polyphenols. Inorg. Chim. Acta 360 (1), 353–359.

Eze, F.N., Jayeoye, T.J., 2021. Chromolaena odorata (Siam weed): a natural reservoir of bioactive compounds with potent anti-fibrillogenic, antioxidative, and cytocompatible properties. Biomed. Pharmacother. 141, 111811.

Faria, P.C.C., Órfão, J.J.M., Pereira, M.F.R., 2004. Adsorption of anionic and cationic dyes on activated carbons with different surface chemistries. Water Res. 38 (8), 2043–2052.
Fayazi, M., Afzali, D., Ghanei-Motlagh, R., Iraji, A., 2019. Synthesis of novel sepiolite–iron oxide–manganese dioxide nanocomposite and application for lead(II) removal from aqueous solutions. Environ. Sci. Pollut. Res. Int. 26 (18), 18893–18903.
Forghani, M., Azizi, A., Livani, M.J., Kafshgari, L.A., 2020. Adsorption of lead (II) and chromium (VI) from aqueous environment onto metal-organic framework MIL-100 (Fe): synthesis, kinetics, equilibrium and thermodynamics. J. Solid State Chem. 291, 121636.
Fu, F., Wang, Q., 2011. Removal of heavy metal ions from wastewaters: a review. J. Environ. Manag. 92 (3), 407–418.
Giraldo, L., Moreno-Piraján, J., 2008. Pb2+ adsorption from aqueous solutions on activated carbons obtained from lignocellulosic residues. Braz. J. Chem. Eng. 25 (1), 143–151.
Groiss, S., Selvaraj, R., Varadavenkatesan, T., Vinayagam, R., 2017. Structural characterization, antibacterial and catalytic effect of iron oxide nanoparticles synthesised using the leaf extract of Cynometra ramiflora. J. Mol. Struct. 1128, 572–578.
Günay, A., Arslankaya, E., Tosun, I., 2007. Lead removal from aqueous solution by natural and pretreated clinoptilolite: adsorption equilibrium and kinetics. J. Hazard. Mater. 146 (1-2), 362–371.
Haji Jasnie, F., 2009. Biological Activities and Chemical Constituents of Chromolaena Odorata (L.) King & Robinson/Faridah Hj Jasnie. University of Malaya.
Holzwarth, U., Gibson, N., 2011. The Scherrer equation versus the'Debye-Scherrer equation'. Nat. Nanotechnol. 6 (9), 534 534.
Jiang, R., Tian, J., Zheng, H., Qi, J., Sun, S., Li, X., 2015. A novel magnetic adsorbent based on waste litchi peels for removing Pb(II) from aqueous solution. J. Environ. Manag. 155, 24–30.
Joshy, D., Chakko, S., Ismail, Y.A., Periyat, P., 2021. Surface basicity mediated rapid and selective adsorptive removal of Congo red over nanocrystalline mesoporous CeO_2. Nanoscale Adv. 3 (23), 6704–6718.
Kapoor, D., Singh, M.P., 2021. 10 - heavy metal contamination in water and its possible sources. In: Kumar, V., Sharma, A., Cerdà, A. (Eds.), Heavy Metals in the Environment. Elsevier, pp. 179–189.
Khulbe, K., Matsuura, T., 2018. Removal of heavy metals and pollutants by membrane adsorption techniques. Appl. Water Sci. 8 (1), 1–30.
Lagergren, S., 1898. Zur theorie der sogenannten adsorption geloster stoffe. K. Sven. Vetensk. 24, 1–39 Handlingar.
Lingamdinne, L.P., Chang, Y.Y., Yang, J.K., Singh, J., Choi, E.H., Shiratani, M., Koduru, J.R., Attri, P., 2017. Biogenic reductive preparation of magnetic inverse spinel iron oxide nanoparticles for the adsorption removal of heavy metals. Chem. Eng. J. 307, 74–84.
Lingamdinne, L.P., Vemula, K.R., Chang, Y.Y., Yang, J.K., Karri, R.R., Koduru, J.R., 2020. Process optimization and modeling of lead removal using iron oxide nanocomposites generated from bio-waste mass. Chemosphere 243, 125257.
Lowe, S., Browne, M., Boudjelas, S., De Poorter, M., 100 of the world's worst invasive alien species: a selection from the global invasive species database, Invasive Species Specialist Group Auckland 2000.
Maiti, D., Mukhopadhyay, S., Devi, P.S., 2017. Evaluation of mechanism on selective, rapid, and superior adsorption of congo red by reusable mesoporous α-Fe_2O_3 nanorods. ACS Sustain. Chem. Eng. 5 (12), 11255–11267.
Mathew, A.T., Hegde, S., Akshaya, K., Kannan, P., Varghese, A., Hegde, G., 2020. MnO_2-Pi on biomass derived porous carbon for electro-catalytic oxidation of pyridyl carbinol. J. Electrochem. Soc. 167 (15), 155513.
McCafferty, E., Wightman, J., Determination of the concentration of surface hydroxyl groups on metal oxide films by a quantitative XPS method, Surf. Interface Anal.: an International Journal devoted to the development and application of techniques for the analysis of surfaces, interfaces and thin films 26(8) (1998) 549-564.
Mehta, D., Mazumdar, S., Singh, S.K., 2015. Magnetic adsorbents for the treatment of water/wastewater—a review. J. Water Process. Eng. 7, 244–265.
Murray, A., Örmeci, B., 2019. Use of polymeric sub-micron ion-exchange resins for removal of lead, copper, zinc, and nickel from natural waters. J. Environmental Sci. 75, 247–254.
Muthukumaran, T., Philip, J., 2016. Effect of phosphate and oleic acid capping on structure, magnetic properties and thermal stability of iron oxide nanoparticles. J. Alloy. Compd. 689, 959–968.
Naranjo, V.I., Hendricks, M., Jones, K.S., 2020. Lead toxicity in children: an unremitting public health problem. Pediatr. Neurol. 113, 51–55.
Obeng-Gyasi, E., 2019. Sources of lead exposure in various countries. Rev. Environ. Health 34 (1), 25–34.
Poulin, S., Franca, R., Moreau-Bélanger, L., Sacher, E., 2010. Confirmation of X-ray photoelectron spectroscopy peak attributions of nanoparticulate iron oxides, using symmetric peak component line shapes. J. Phys. Chem. C 114 (24), 10711–10718.
Rajan, A., Sharma, M., Sahu, N.K., 2020. Assessing magnetic and inductive thermal properties of various surfactants functionalised Fe3O4 nanoparticles for hyperthermia. Sci. Rep. 10 (1), 1–15.
Reck, B.K., Graedel, T.E., 2012. Challenges in metal recycling. Science 337 (6095), 690–695.
Ricci, A., Olejar, K.J., Parpinello, G.P., Kilmartin, P.A., Versari, A., 2015. Application of Fourier Transform Infrared (FTIR) spectroscopy in the characterization of tannins. Appl. Spectrosc. Rev. 50 (5), 407–442.
Roy, A., Murthy, H.A., Ahmed, H.M., Islam, M.N., Prasad, R., 2022. Phytogenic synthesis of metal/metal oxide nanoparticles for degradation of dyes. J. Renew. Mater. 10 (7), 1911.
Sajeev, T., Sankaran, K., Suresh, T., Are alien invasive plants a threat to forests of Kerala, KFRI occasional papers, Forest Health Programme Division. Kerala Forest Research Institute, Peechi (2012).
Simonin, J.P., 2016. On the comparison of pseudo-first order and pseudo-second order rate laws in the modeling of adsorption kinetics. Chem. Eng. J. 300, 254–263.
Smith, D.W., 1977. Ionic hydration enthalpies. J. Chem. Educ. 54 (9), 540.
Thomas, J.M., Tricker, M.J., 1975. Electronic structure of the oxides of lead. Part 2.—An XPS study of bulk rhombic PbO, tetragonal PbO, β-PbO_2 and Pb_3O_4. J. Chem. Soc. Faraday Trans. 2 71 (0), 329–336.
Usman, H., Abdulrahman, F., Usman, A., 2009. Qualitative phytochemical screening and *in vitro* antimicrobial effects of methanol stem bark extract of Ficus thonningii (Moraceae). Afr. J. Tradit. Complement. Altern. Med. 6 (3), 289–295.
Vijayaraghavan, K., Rajkumar, J., Bukhari, S.N.A., Al-Sayed, B., Seyed, M.A., 2017. Chromolaena odorata: a neglected weed with a wide spectrum of pharmacological activities. Mol. Med. Rep. 15 (3), 1007–1016.
Wang, X., Zhao, Y., Jiang, X., Liu, L., Li, X., Li, H., Liang, W., 2018. *In-situ* self-assembly of plant polyphenol-coated Fe_3O_4 particles for oleaginous microalgae harvesting. J. Environ. Manag. 214, 335–345.
Wani, A.L., Ara, A., Usmani, J.A., 2015. Lead toxicity: a review. Interdiscip. Toxicol. 8 (2), 55–64.
Xu, Z., Gu, S., Rana, D., Matsuura, T., Lan, C.Q., 2021. Chemical precipitation enabled UF and MF filtration for lead removal. J. Water Process. Eng. 41, 101987.
Yusefi, M., Shameli, K., Ali, R.R., Pang, S.W., Teow, S.Y., 2020. Evaluating anticancer activity of plant-mediated synthesized iron oxide nanoparticles using Punica granatum fruit peel extract. J. Mol. Struct. 1204, 127539.
Zhang, W., Yang, J., Wu, X., Hu, Y., Yu, W., Wang, J., Dong, J., Li, M., Liang, S., Hu, J., 2016. A critical review on secondary lead recycling technology and its prospect. Renew. Sustain. Energy Rev. 61, 108–122.